KeAi

CHINESE ROOTS
GLOBAL IMPACT

#### Contents lists available at ScienceDirect

# Petroleum Science

journal homepage: www.keaipublishing.com/en/journals/petroleum-science



# Original Paper

# Thin layer identification using a theoretical X-ray logging while drilling (LWD) density imaging tool



Wen-Bin He<sup>a</sup>, Ji-Lin Fan<sup>a,b</sup>, Qiong Zhang<sup>a,\*</sup>, Ya Jin<sup>c</sup>, Wei Yuan<sup>c</sup>, Quan-Wen Zhang<sup>c</sup>

- <sup>a</sup> Department of Control Science and Engineering, School of Automation Engineering, University of Electronic Science and Technology of China, Chengdu, 611731, Sichuan, China
- <sup>b</sup> China National Logging Corporation, Xi'an, 710077, Shaanxi, China
- <sup>c</sup> China Oilfield Services Limited, Sanhe, 065201, Hebei, China

#### ARTICLE INFO

#### Article history: Received 13 January 2025 Received in revised form 10 April 2025 Accepted 25 May 2025 Available online 28 May 2025

Edited by Meng-Jiao Zhou

Keywords: LWD density imaging X-ray tool design Thin layer identification

# ABSTRACT

With the increasing demand for oil exploration and subsurface resource development, density imaging plays an increasingly important role in identifying thin layers. However, conventional density imaging tools are limited by poor vertical resolution and therefore suffer from errors in accurately estimating the thickness and relative dip angle of thin layers. This affects the accurate evaluation of thin layer oil and gas reserves. To address this issue, this study evaluates the feasibility of employing novel methods based on advanced tool design. First, an electronically controllable X-ray source is selected to replace the traditional Cs-137 source, aiming to improve the tool's vertical resolution while reducing the radioactive risks commonly associated with chemical sources. Simulation results show that the X-ray tool provides sufficient depth of investigation with better vertical resolution while maintaining the same level of measurement sensitivity. Once the tool design is established, Fisher's optimal segmentation method is improved to enhance the estimation of thin layer thickness and relative dip angle. This is completed by transforming identifying thin layer interface into a mathematical clustering problem. The thin layer interface is fitted using the nonlinear least squares method, which enables the calculation of its parameters. The results demonstrate a 38.5% reduction in RMSE (root mean square error) for thin laver thickness and a 33.7% reduction in RMSE for relative dip angle, demonstrating the superior performance of enhanced X-ray tool in thin layer identification. This study provides a new perspective on the design of density imaging tools and assessment of thin layer, which can help in future thin layer hydrocarbon reserves evaluation and development decisions.

© 2025 The Authors. Publishing services by Elsevier B.V. on behalf of KeAi Communications Co. Ltd. This is an open access article under the CC BY-NC-ND license (http://creativecommons.org/licenses/by-nc-nd/4.0/).

#### 1. Introduction

As the global demand for oil exploration continues to grow, the accurate identification and real-time monitoring of formation characteristics become particularly important, especially in the development of thin inter-bedded layers (Geng et al., 2022; Pang et al., 2022), deep layers (Bai and Cao, 2014; Peng et al., 2016), and low-permeability reservoirs (Hu et al., 2018; Kang et al., 2022) in complex reservoir environments. Logging while drilling (LWD) density measurements have been widely used in oil and gas exploration because they can obtain formation density data in

1983). In particular, LWD density imaging can measure the formation density distribution in all directions around the well, helping explorers accurately identify formation features (Best et al., 1995; Zhu et al., 2019) and determine reservoir properties (Sun et al., 2021; Yuan et al., 2022). However, with the global emphasis on environmental safety, density logging is gradually moving towards source-less density (Zhang et al., 2023). The X-ray source has shown excellent potential in replacing Cs-137 source for formation density measurement because of its electronically controllable characteristics. In 2014, Badruzzaman (2014) initially investigated the feasibility of X-ray source density logging. In 2018, Schlumberger Simon et al. (2018) introduced the first commercially available four-detector X-ray density logging tool, noting

that X-ray density tool provides higher sensitivity and vertical

real-time during drilling (Eldert et al., 2020, John and Turvill,

<sup>\*</sup> Corresponding author.

E-mail address: zhanqio@uestc.edu.cn (Q. Zhang).

resolution for formation density measurement. Using the energy spectrum generated by its X-ray generator, Wu et al. (2022) explored the application of controllable X-ray sources in downhole density measurements through numerical simulations, providing references for the design of related instruments. Singhal et al. (2018) proposed an X-ray based high-pressure density and mass flow sensor for real-time monitoring of drilling fluids in highpressure environments. Further exploration of X-ray digital radiography techniques by Wang and Zhang (2023) and Li et al. (2023) evaluated the performance of flexible detectors such as CsPbBr3 crystal detectors in X-ray imaging. Recently, the method proposed by Fan et al. (2024), which combines X-ray sources and gamma detectors to calculate cement density with a controllable error margin, provides a new technical means for cement quality assessment. These research demonstrate the excellent potential of X-ray technology for density measurement and analysis capabilities in density logging while drilling. The successful application of these technologies demonstrates the significant potential of X-ray technology in LWD.

X-rays have also found some application in imaging, and for LWD density images, accurate identification of formation interfaces is critical for the assessment of thin layer thickness and relative dip angle. Lanning and Johnson (1983) pioneered the use of Walsh transform to analyze log data to detect formation boundaries. Later, Wang et al. (2013) introduced the influencing factors and basic theories of automated identification of LWD density imaging, providing a theoretical basis for automated data analysis. Shao et al. (2013) proposed a fast forward algorithm for LWD gamma logging under the condition of complex formation interface and well trajectory, as well as a key calculation method for determining formation interface using gamma forward in real time. Xie et al. (2014), Cheng and Zou, 2015 and Mukherjee et al. (2016) studied the automatic identification method of formation interface based on edge detection, Hough transform, and wavelet transform. These methods usually require elaborate image processing pipelines and require high performance of computing devices. To address this problem, Gupta et al. (2019) and others proposed algorithms for formation interface identification based on a fully convolutional neural network model (FCN). However, the method faces challenges in practical applications, such as algorithm parameter selection, high-resolution data acquisition, and theoretical background combination. To overcome these challenges, this manuscript employs the Fisher optimal segmentation method (FOSM) (Fisher, 1958), which transforms the interface recognition problem into a clustering problem in mathematical form, and realizes the interface recognition of formation. Specifically, the FOSM is applied to optimize the segmentation points at the formation interfaces by minimizing the density data intraclass scatter, which enables the distinction of different formation zones.

Based on this, the structure of this manuscript is organized as follows: In Section 2, the design of the X-ray tool is introduced. Xray tool is developed by replacing the chemical source with an Xray source. The optimization of source spacing is conducted, ensuring that the tool maintains sufficient depth of investigation (DOI) and good density sensitivity while improving vertical resolution. Section 3 presents the application of Fisher's optimal segmentation method to the density images obtained from both the X-ray and conventional LWD tools. This method is employed to estimate the thickness and relative dip angle of thin layers, key indicators for thin layer recognition. In Section 4, the results and discussion are presented, demonstrating that the X-ray tool significantly improves the accuracy of thin layer thickness and relative dip angle calculations compared to the conventional tool, based on two different models. Finally, Section 5 concludes the paper, summarizing the main findings and contributions.

#### 2. X-ray density tool design

Geant4 (Agostinelli et al., 2003; Allison et al. 2006, 2016) is a widely used and open source Monte Carlo particle transport tool that supports the transport simulation of various particles (such as neutrons, photons, electrons, etc.). It is widely used in particle physics experiments, medical physics, radiation protection, radiation measurement, nuclear well logging and other fields. In this study, Geant4 is used to design and validate an X-ray tool (X\_tool), and optimize the detector-to-source distance based on density sensitivity to ensure that the tool has sufficient DOI. This improves the tool's vertical resolution and ability to identify thin layers.

#### 2.1. Tool model construction

First, a gamma tool model, denoted as G\_Tool, is established using Geant4, shown schematically in Fig. 1. Fig. 1(a) shows the structure of the G\_tool, which is mainly composed of Cs-137 source, short- and long-spaced NaI detectors, detector shell and tungsten-nickel-iron shield and other key components. The source-to-detector distance of the long- and the short-spaced detectors are 380 mm and 183 mm, respectively. The short-spaced NaI crystal has a size of  $\phi 20.32$  mm  $\times$  19.05 mm, while the long-spaced NaI crystal measures  $\phi 20.32$  mm  $\times$  57.15 mm. The tool has an external diameter of 304 mm. Fig. 1(b) shows the schematic of X\_tool, where the Cs-137 source is replaced by an X-ray source.

Fig. 1(c) presents the energy spectra of X\_tool and G\_tool, highlighting a distinct difference in their spectral characteristics. To reduce the influence of lithology on density measurements, X\_tool employs a density energy window ranging from 140 to 250 keV, whereas G\_tool operates within a window of 200–410 keV. To verify the accuracy of the G\_tool model, simulated results are compared with experimental measurements from 13 test pits, as shown in Fig. 2. The results indicate that the density energy windows for both the short- and long-spaced detectors exhibit a high degree of consistency between simulation and measurement, with statistical errors remaining within 5%. These findings confirm the reliability and correctness of the model.

Based on the validated G\_tool, the X\_tool model is designed by replacing the 0.662 MeV monoenergetic Cs-137 source with an X-ray spectra of an end energy 350 keV. The X-ray energy distribution can be referred to Schlumberger's X-ray energy spectrum (Simon et al., 2018). Moreover, considering that the intensity of the X-ray source is an order of magnitude higher than that of the 7.4  $\times$  10 $^{10}$  Bq Cs-137 source, the intensity of the X-ray source is 62.9  $\times$  10 $^{10}$  Bq.

Density sensitivity is employed as an important parameter to evaluate the performance of density tools. It refers to the change in the logarithm of density window photon count caused by a unit density change. The equation is shown as Eq. (1), where N is the density window photon count and  $\rho$  is the formation density.

$$S = \left| \frac{\partial (\ln N)}{\partial \rho} \right| \times 100\% \tag{1}$$

Fig. 3 shows the sensitivity comparison of density measurement of two tools under different densities. It shows that under the same source spacing condition, the sensitivity of X\_Tool is significantly higher than that of G\_tool. Although the photon energy is lower than that of the Cs-137 source, the number of particles recorded by the X\_tool detector is higher, mainly because the intensity of X-ray is one order of magnitude higher than Cs-137.

Since tool sensitivity to formation decreases as detector-tosource distance reduces, the source-detector spacing of the

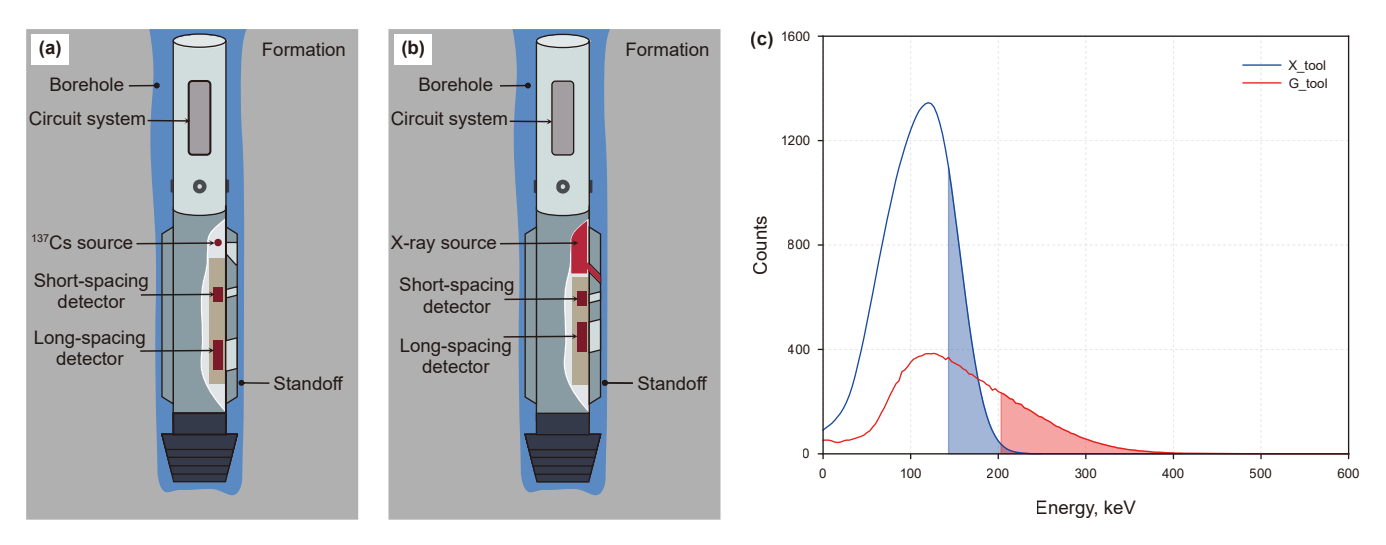


Fig. 1. Schematic of tools for two different density sources.

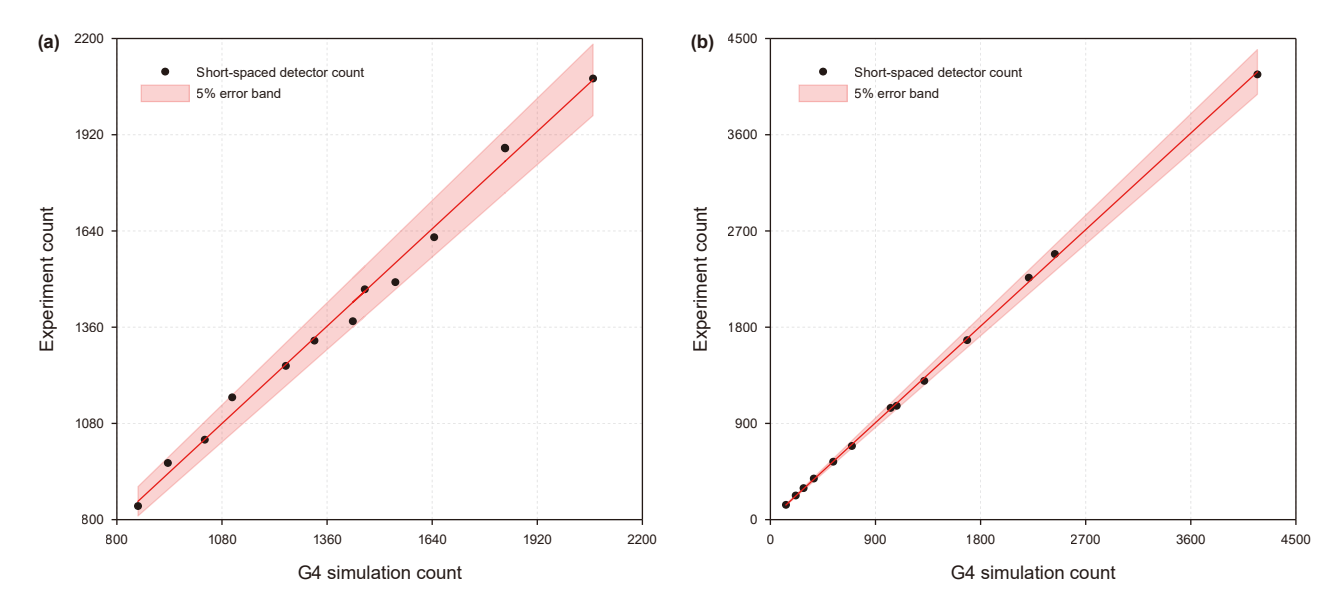


Fig. 2. Comparison of density window counts between simulation and measurement.

X\_tool can be further optimized on the premise of ensuring that the density sensitivity of the X\_tool is no less than that of the G\_tool. This could provide several advantages such as more fitting space for the X-ray tube and more flexible tool design. Furthermore, the appropriate source-detector spacing adjustment can improve the vertical resolution of the tool, this helps enhancing the ability of the tool in identifying thin layers.

## 2.2. Optimization of X-ray source spacing

Using the X\_tool model, the source spacing of the short- and long-spaced detectors are adjusted to achieve optimized performance. Among them, the source spacing of the long-spaced detector is gradually adjusted from 380 mm to 240 mm, and the source spacing of the short-spaced detector is gradually adjusted from 183 mm to 113 mm. Change gradually in decreasing steps. At the same time, under each source spacing, the formation density is adjusted, and the detection energy spectrum counts under different density conditions are simulated and recorded, so as to obtain the response relationship between density window counts

and formation density under the condition of source spacing. Finally, the density sensitivity under different detector source spacing conditions are obtained, as shown in Fig. 4.

From Fig. 4, it is evident that the density sensitivities of both the short- and long-spaced detectors decrease as the source spacing decreases, exhibiting a clear linear relationship with the source spacing. Fig. 3 shows that, without adjusting the source spacing, the density sensitivities of both the short- and long-spaced detectors of X\_tool are higher than those of G\_tool. Therefore, to ensure that the density sensitivity of X\_tool is not lower than that of G\_tool, the minimum long- and short-source spacing for X\_tool can be determined based on the linear relationship. Under these source spacing conditions, the density sensitivity of X\_tool becomes comparable to that of G\_tool. According to Fig. 3, the density response sensitivities of the short- and long-spaced detectors of G\_tool are 0.450 and 1.748, respectively. By combining this with the fitting relationship shown in Fig. 4, it can be concluded that the short source spacing of X\_tool should exceed 112.987 mm, while the long source spacing should exceed 258.952 mm.

In view of the actual design of the tool, a longitudinal shielding



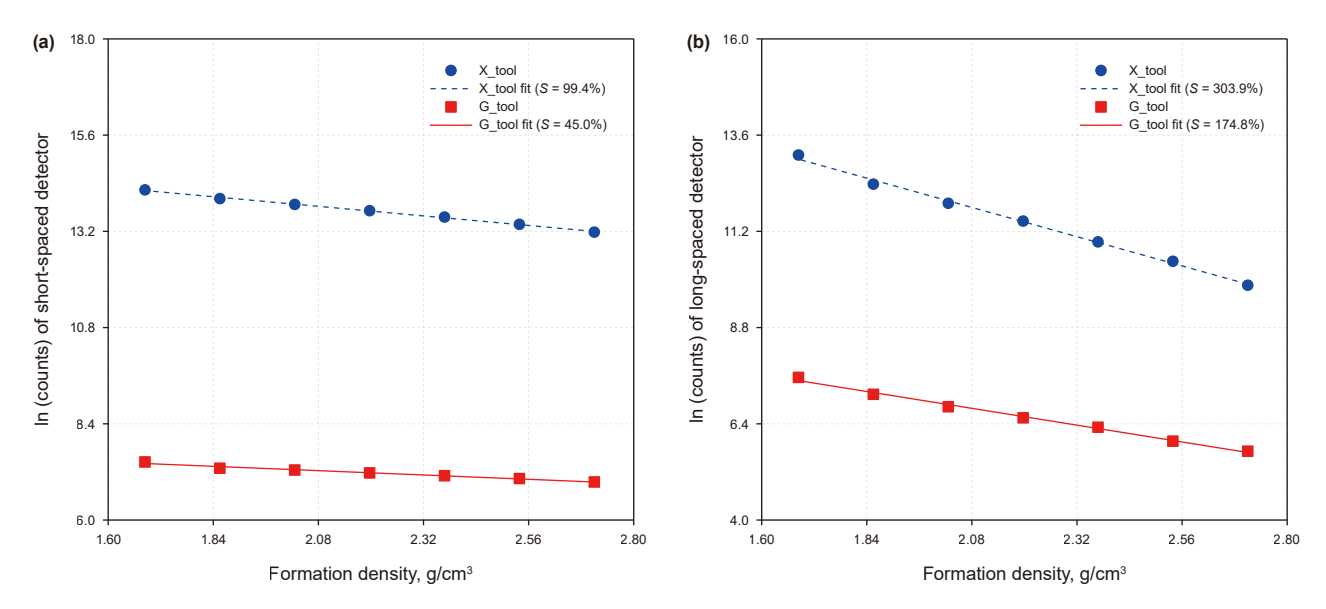


Fig. 3. Comparison of density measurement sensitivity of two tools.

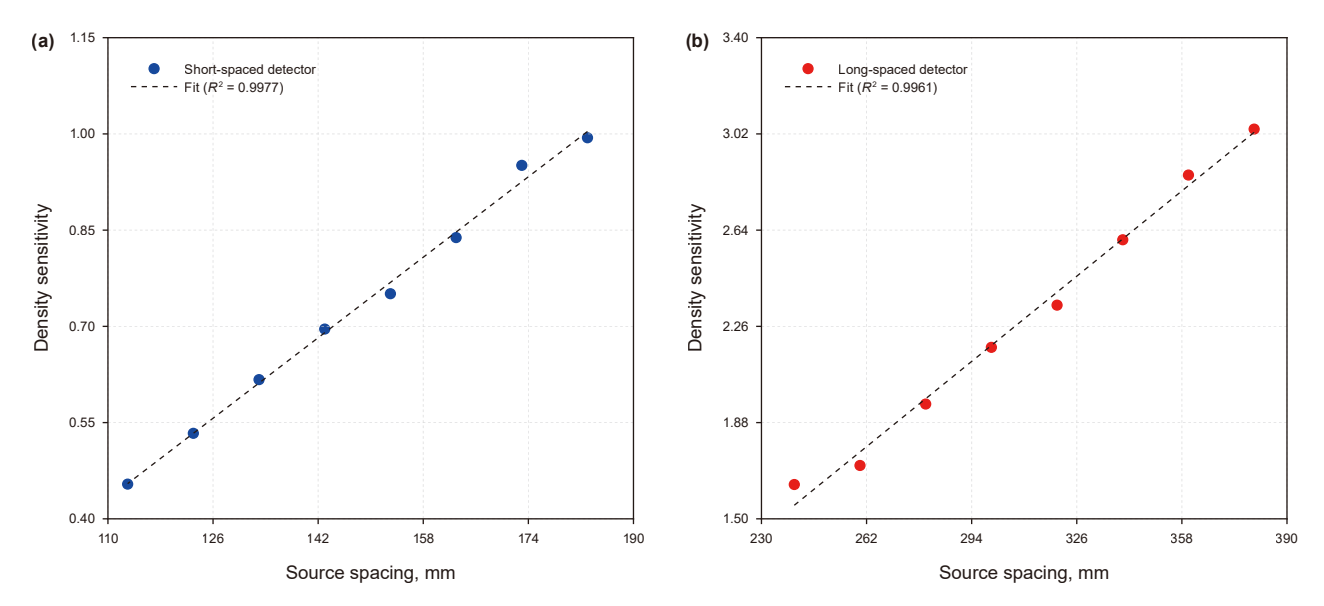


Fig. 4. Variation of density sensitivity with source spacing for short- and long-spaced detectors.

body is set between the source and short-spaced detector, which imposes certain restrictions on the optimization of the short source spacing. After comprehensive analysis, the maximum adjustable distance of the short-spaced detector is 45 mm. On this basis, the optimized source spacing of X\_tool is finally shown in Table 1, where the source spacing of short- and long-spaced detectors is 138 mm and 260 mm, respectively.

To validate the effectiveness of the new source spacing, a simulation-based comparison of the DOI is conducted for the optimized tool. As shown in Fig. 5(a), the DOI of the long-spaced

**Table 1**Source spacing of the X\_tool after optimization.

Source spacing	G_tool	X_tool
Short source spacing	183 mm	138 mm
Long source spacing	380 mm	260 mm

detector for both tools is evaluated under standard limestone formation conditions. It can be observed that the X-ray longspaced detector achieves a DOI of approximately 8.5 cm, which is sufficient for acquiring formation information in LWD environments. Furthermore, to quantitatively assess the improvement in vertical resolution, formation models with different thin layer thicknesses (25, 20, 15, 10, and 5 cm) are constructed, and the tool responses are simulated to analyze the capability of identifying formation boundaries under varying conditions. The simulation results, as presented in Fig. 5(b) and (c), where the black solid lines represent the formation density values defined by the model. The blue and red dashed lines correspond to the simulated responses of G\_tool and X\_tool, respectively. All curves are aligned based on the midpoint between the short- and long-spaced detectors as the reference depth. As shown in the figures, the vertical resolution of X\_tool is approximately 15 cm, while that of G\_tool is around 20 cm. These findings further confirm the superior vertical

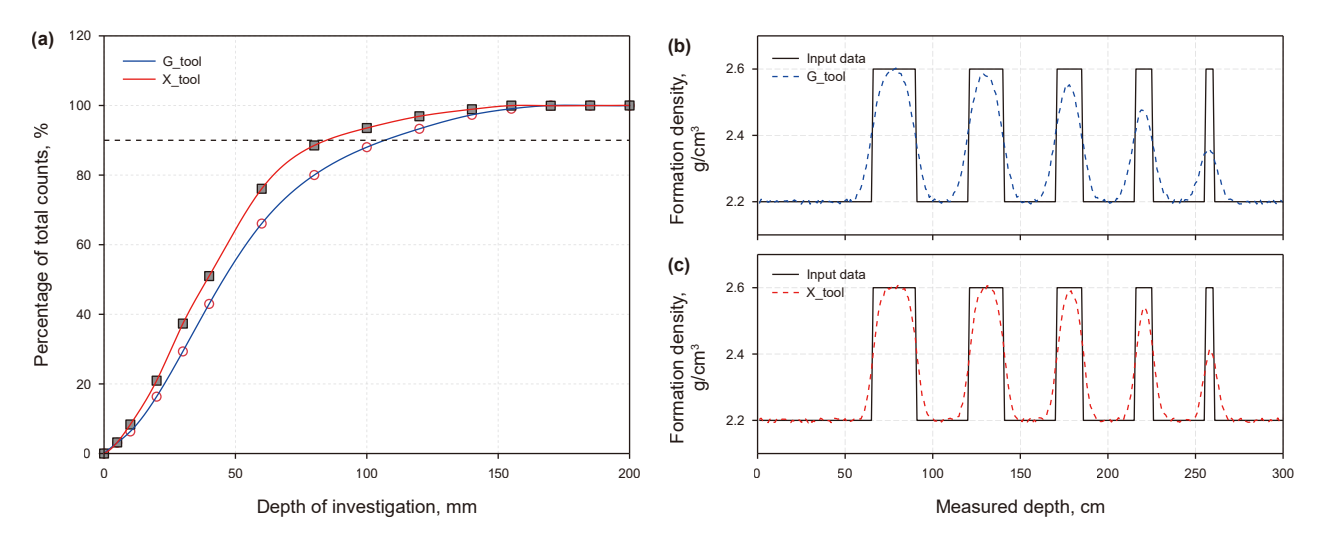


Fig. 5. DOI comparison and vertical resolution simulation results for X\_tool and G\_tool.

resolution of X\_tool, which is primarily attributed to its reduced source-to-detector spacing.

## 2.3. Density calculation

In order to verify the performance of the improved X\_tool, its density response is evaluated through simulation under different logging environments. Specifically, the formation is set as limestone with porosity varying between 0% and 40% (density range:  $2.112-2.710~\rm g/cm^3$ ); the borehole fluids are set as water, light mud (density  $1.440~\rm g/cm^3$ ) and heavy mud (density  $2.440~\rm g/cm^3$ ), and the standoff is set from 0 to 20 mm. By constructing the simulation databased including the above models, we fit and obtain the compensation density response of the two tools, as shown in Fig. 6. The horizontal axis represents the density, difference between the short- and long-spaced detectors and the vertical axis is the density correction added to the long -spaced detector apparent densities when calculating the final formation density.

To quantitatively evaluate the accuracy of the tools, we used a test set covering a range of formation porosities and mud densities. The mean absolute error (MAE) and root mean square error (RMSE) are employed as evaluation metrics, defined as follows:

$$MAE = \frac{1}{n} \sum_{i=1}^{n} |\rho_i - \widehat{\rho}_i|$$
 (2)

$$RMSE = \sqrt{\frac{1}{n} \sum_{i=1}^{n} (\rho_i - \widehat{\rho}_i)^2}$$
 (3)

The error results are summarized in Table 2. For G\_tool, the MAE and RMSE of the formation density are 0.0146 and 0.0148 g/cm<sup>3</sup>, respectively. In contrast, X\_tool achieves improved accuracy, with an MAE of 0.0140 g/cm<sup>3</sup> and an RMSE of 0.0143 g/cm<sup>3</sup>. These results indicate that X\_tool delivers more accurate and reliable formation density measurements compared to G\_tool.

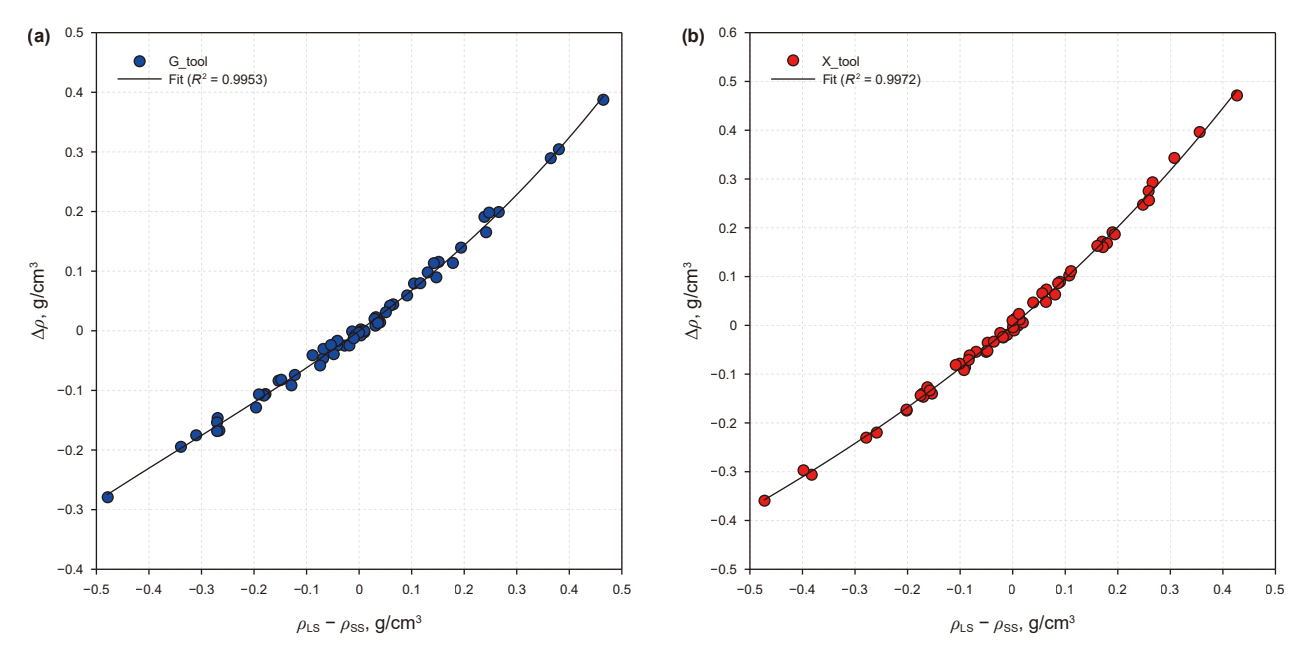


Fig. 6. Fitting compensation density correction.

**Table 2**Comparison of formation density error between G\_tool and X\_tool.

Error	G _tool	X_tool
MAE	0.0146 g/cm <sup>3</sup>	0.0140 g/cm <sup>3</sup>
RMSE	0.0148 g/cm <sup>3</sup>	0.0143 g/cm <sup>3</sup>

## 3. Thin layer identification

Since the LWD tool can collect density data in 16 sectors around the well while the tool is rotating, it is possible to utilize the density data in 16 sectors around the well to realize the imaging of formation density. Firstly, the boundaries of thin layers can be recognized by the formation density image, and then the thickness and relative dip angle of thin layers can be calculated.

Fig. 7 illustrates the 16 sector density values and their density images simulated by the X\_tool model while passing through the high and low density layers. The density value and composition of the high and low density layer are shown in Table 3. The thicknesses of the high- and low-density layers are set to 50, 40, 30, 20, and 10 cm, with a specific relative dip angle to the borehole. The traces in the figure show, from left to right, the density of each sector in azimuths ranging from 11.25° to 348.75° in 22.5° increments, with the red dashed line indicating the 16-sector density curve, and the black boxed lines indicating the values of the formation density under each azimuth under the forward model. The rightmost display is the density image obtained by circumferential interpolation of the left 16 sector densities.

From the density image, it can be seen that when the tool crosses the thin layers of high and low density, the image shows obvious sinusoidal curve characteristics. This is because when there is an interface between the layers, there is a difference in the density of the formations above and below the interface, which is reflected in the density image as the sinusoidal response curve in

Fig. 7. By analyzing the sinusoidal features in the LWD density image, the relative dip angle  $\theta$  of the thin layer with respect to the borehole and its thickness T can be deduced (Yin et al., 2008), as shown in Fig. 8:

$$\theta = \tan^{-1} \left( \frac{H}{D + 2\Delta D} \right) \tag{4}$$

$$T = L \cdot \sin(90^\circ - \theta) \tag{5}$$

where H represents the amplitude of the sinusoidal curve in the density image. D is the diameter of the hole;  $\Delta D$  represents the range of density imaging response to formation density in the direction perpendicular to the well axis (i.e., the DOI). L is the distance value of the sine curve in the direction of the well axis in the density image.

# 3.1. Fisher optimal segmentation method

Based on the simulation model constructed in the previous section and the equations for calculating the relative dip angle and thickness of thin layers, a method is developed to identify thin layer interfaces in each azimuth using the FOSM, enabling the accurate evaluation of relative dip angle and thickness in the density image. This method consists of three main steps, as shown in Fig. 9. First, the 16-sector density matrix data are interpolated to enhance resolution and obtain a finer density distribution. Next, key points on the thin layer interfaces in each azimuth of the interpolated density matrix are identified using FOSM to delineate thin layer boundaries. Finally, the nonlinear least squares (NLS) method is applied to fit the identified thin layer interfaces in order to achieve a quantitative assessment of the relative dip angle and thickness.

The goal of FOSM is to minimize the total sum of squared deviations of the layers after stratification so that the differences within the layers are minimized and the differences between the

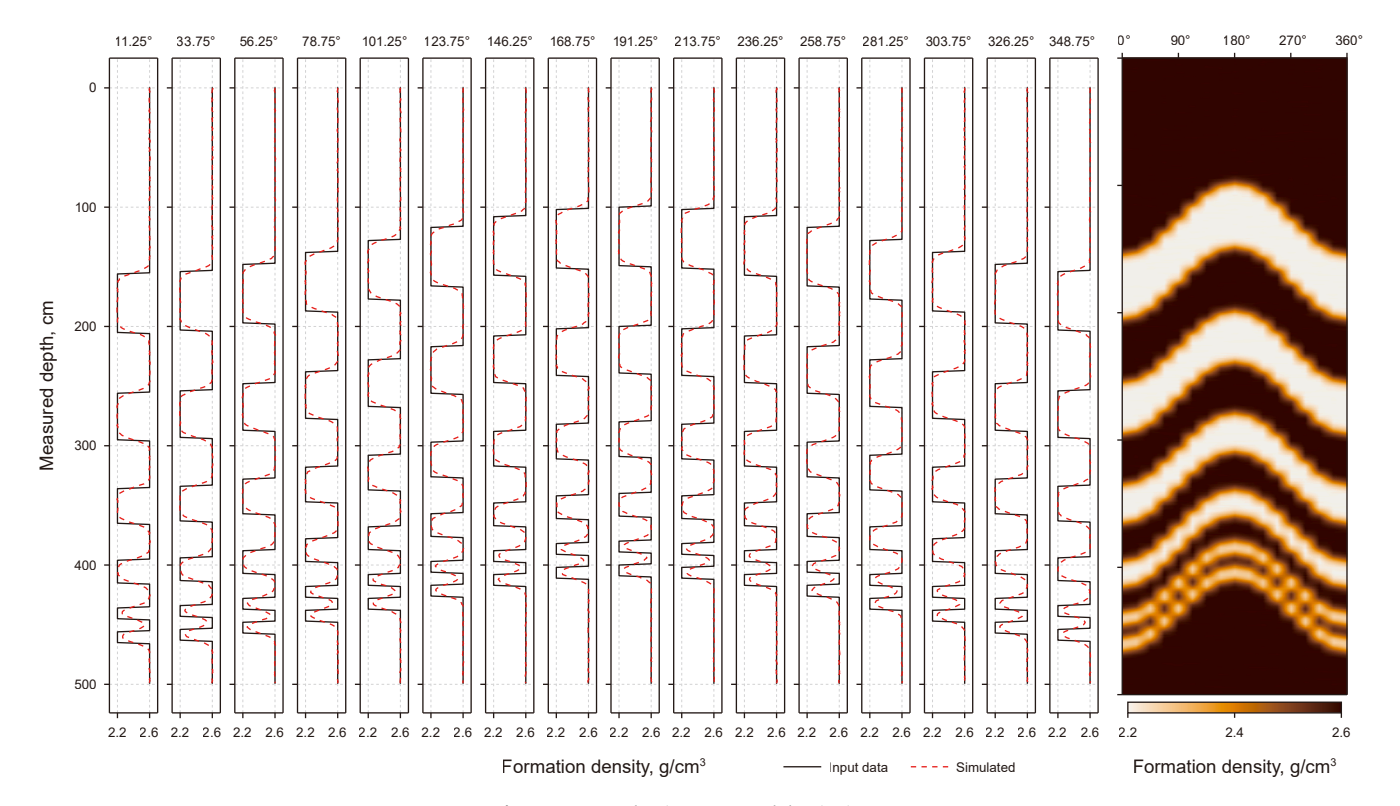
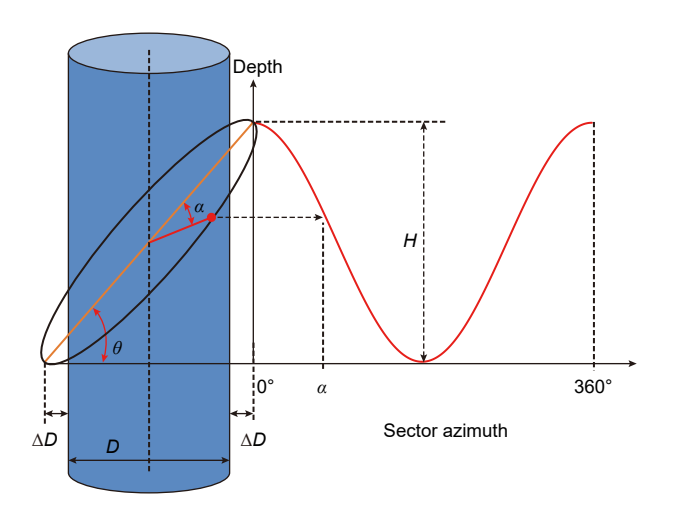


Fig. 7. 16-sector density curves and density images.

**Table 3**Material composition of the high and low density layers.

Composition	Low density layer (2.20 g/cm <sup>3</sup> )	High density layer (2.60 g/cm <sup>3</sup> )
SiO <sub>2</sub>	21.00%	45.00%
CaCO <sub>3</sub>	50.00%	50.00%
$H_2O$	29.00%	5.00%



**Fig. 8.** Schematic diagram of the formation interface and the sinusoidal response curve of the interface.

layers are maximized. This clustering method of ordered rules can segment the data efficiently. In applying the Fisher optimal segmentation method, the density image is represented as a data matrix:  $R \in R^{m \times n}$ , where m is the depth dimension and n is the azimuth dimension. For each column j (i.e., an azimuth), the density data are  $\{\rho_j(1), \rho_j(2), \cdots, \rho_j(m)\}$ . By Fisher's optimal segmentation method, the goal is to find a set of k+1 segmentation

points  $\{s_1, s_2, \cdots, s_{k+1}\}$  that segment each azimuthal profile into k thin layer bins and minimize the density difference within each bin and maximize the density difference between the bins. Therefore, the procedure of the optimal segmentation method for thin layer interface identification are as follows.

1. Define the interval diameter. Denote the *t* ordered densities of a thin interval at orientation as *j* and the mean vector as

$$\overline{\rho_j} = \frac{1}{m - i + 1} \sum_{y=i}^{m} \rho_j(x) \tag{6}$$

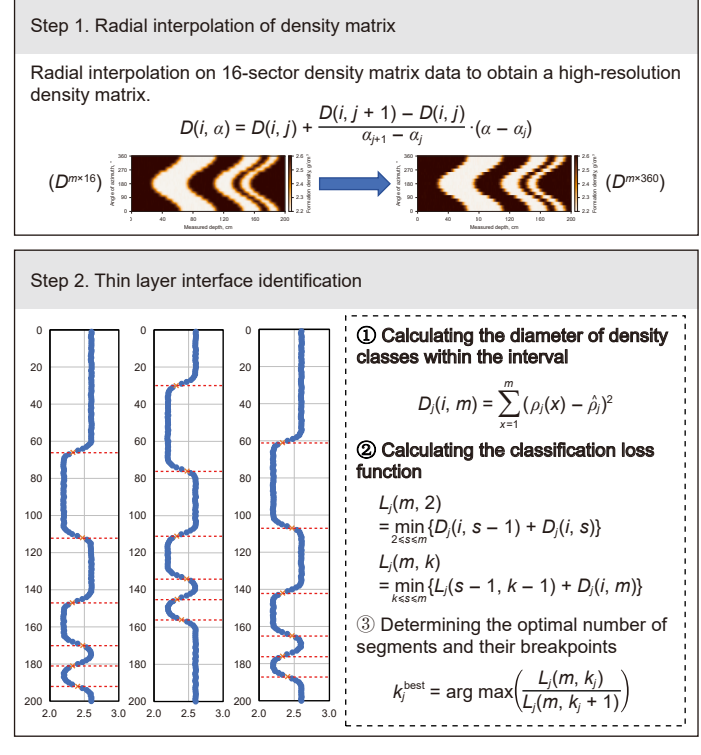
Then the class diameter of this vector is

$$D_{j}(i,m) = \sum_{x=i}^{m} \left( \rho_{j}(x) - \overline{\rho_{j}} \right)^{2} \tag{7}$$

2. Compute the classification loss. The recursive equation of the classification loss function is as follows:

$$\begin{cases}
L_{j}(m,2) = \min_{2 \le s \le m} \left\{ D_{j}(i,s-1) + D_{j}(i,s) \right\} \\
L_{j}(m,k) = \min_{k \le s \le m} \left\{ L_{j}(s-1,k-1) + D_{j}(i,m) \right\}
\end{cases}$$
(8)

where (m, k) is a partition that clusters the m ordered densities



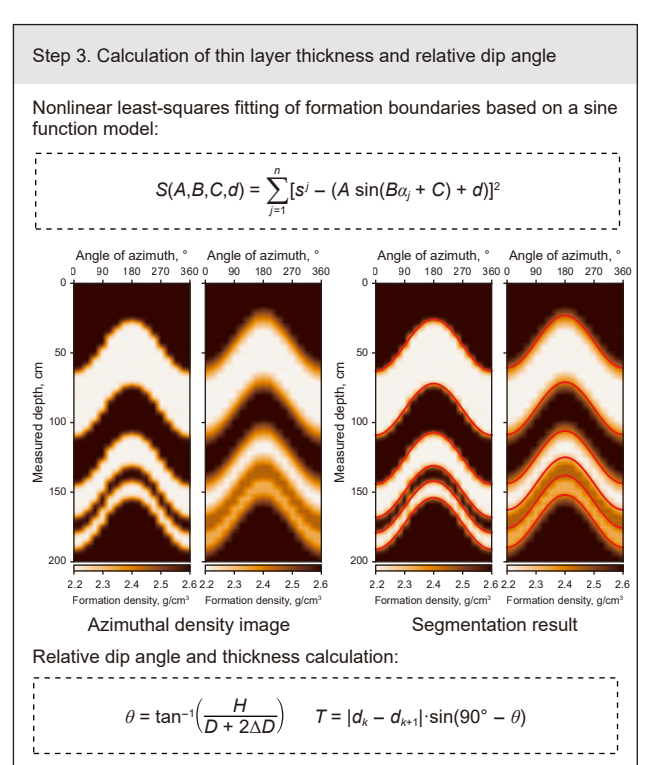


Fig. 9. An overview of formation interface identification using Fisher optimal segmentation method.

under m orientation into k classes;  $L_j(m,k)$  is the loss function of (m,k) partition. According to Eq. (8), the classification loss function table for 2-partition to k-partition can be derived.

3. Determine the optimal number of layers  $k_j$ . The inflection point in the trend graph of  $L_j(m,2)$  changing with the optimal number of layers k is the optimal number of layers. The loss function ratio  $\delta_j$  can be calculated, and the larger the ratio is, the better the division into k segments than k+1 segments.

$$\delta_j = \frac{L_j(m,k)}{L_j(m,k+1)} \tag{9}$$

After determining the optimal number of layered layers and the position of the interface of the thin layer under each orientation, the interface curve of the thin layer, i.e., the sinusoidal curve shown in Eq. (10), is finally obtained by nonlinear least-squares fitting.

$$S(A, B, C, d) = \sum_{r=i}^{m} \left[ \left\{ s^{i} \right\} - \left( A \sin \left( B \alpha_{j} + C \right) + d \right) \right]^{2}$$
 (10)

where, A,B,C,d is the coefficient of the sine curve obtained by fitting, and  $s^j$  is the position of the thin layer interface determined in all directions. The interfacial curve parameters of each interface are finally obtained, and then the thickness and relative dip angle of the thin layer can be calculated from the parameter information of these curves.

#### 4. Result and discussion

In this section, the advantages of the X\_tool over the conventional G\_tool for thin layer identification are verified by evaluating the thickness and relative dip angle of the thin layers. This is achieved by constructing two thin layered formation models, then employing FOSM to identify the thickness and relative dip angle of the thin layers. Results are then compared between two tools.

# 4.1. Thin layer thickness evaluation

The density response of 16 sectors with different layer thicknesses (40, 30, 20, and 10 cm) is simulated at 60° relative dip. Subsequently, the density images under the corresponding conditions are obtained, as shown in Fig. 10. The results indicate a significant difference in boundary clarity and vertical resolution between the two tools. In the image obtained from X\_tool, formation boundaries are more distinct, with narrower transition zones and sharper interface transitions. In contrast, the image from G\_tool presents relatively blurred boundaries with wider transition areas, resulting in lower boundary distinguishability.

Fig. 11 illustrates the results of formation boundary segmentation using the FOSM, with fitted sine curves indicating the identified interfaces. The thicknesses of different layers are clearly distinguishable in the image, and the distances between the curves accurately reflect the variations in layer thickness. Additionally, the positions of the fitted curves align well with the actual thin-layer boundaries. Notably, even when the thin layer thickness is reduced to 10 cm—approaching or slightly below the vertical resolution of the tool—FOSM is still capable of segmenting the layer regions and extracting structural contours to a certain extent. This suggests that the method retains a degree of applicability under low-resolution conditions. The comparison between the layer thicknesses calculated using Eq. (4) and the preset simulation values is presented in Table 4.

As shown in Table 4, the calculation errors for layer thickness in

both tools increase as the thickness decreases. This is because, when the thin layer thickness is small, the measured density values are more susceptible to interference from adjacent layers, making it difficult to accurately reflect the actual formation conditions. Consequently, the calculation of thin layer thickness based on density images results in larger errors. It can also be observed that, under all thin layer thickness conditions, the calculation errors of X\_tool are consistently lower than those of G\_tool. This is attributed to the shorter source spacing of X\_tool, which provides relatively higher vertical resolution and reduces the influence of adjacent layers. Table 5 compares the results of the two tools, showing that the RMSE of thin layer thickness calculated by X\_tool is 0.512 cm, while that of G\_tool is 0.834 cm. The RMSE of X\_tool is reduced by 38.5%, demonstrating its better performance in thin layer identification.

## 4.2. Thin layer dip evaluation

Similarly, the density imaging results of the two tools under different relative dip angles are also simulated, as shown in Fig. 12. Fig. 12(a) shows the schematic diagram of the simulation model, in which the strata includes formations with relative dip angles of  $15^{\circ}$ ,  $30^{\circ}$ ,  $45^{\circ}$  and  $60^{\circ}$ . Fig. 12(b) shows the comparison results of density images.

Fig. 13 shows the interface identification results of the two tool density images under different relative dip angle models. The relative dip angle is calculated by combining with Eq. (4), and the results are shown in Table 6.

As can be seen in Table 6, as the relative dip angle of the thin layer increases, the calculation error of the relative dip angle of the thin layer tends to increase for both tools. This is because the tool has a certain DOI, when the thin layer dip angle is larger, the thin layer density interaction area enlarges as the amplitude deviation of the interface curve increases, therefore, obtaining the thin layer relative dip angle through the amplitude will produce a larger error. Meanwhile, the error of the thin layer relative dip angle of X\_tool is lower than that of G\_tool pertaining to all thin layer relative dip angles. This is due to the relatively smaller DOI of X\_tool and the smaller area where thin layer densities interact. Results of the two tools are compared in Table 7, where the RMSE calculated by the relative dip angle of thin layers is 1.275° for X\_tool and 1.946° for G\_tool, and the RMSE of X\_tool is reduced by 38.5%, which indicates that the X\_tool performs better in identifying thin layers.

## 5. Conclusions

Based on an actual LWD density tool, this work replaces the traditional gamma source with a controllable X-ray source and optimizes the source spacing of the short- and long-spaced detectors in the X\_tool without compromising measurement sensitivity. In addition, the FOSM is employed to identify thin layer interfaces in the density image, and the thin layer thickness as well as the relative dip angle are calculated. Finally, the accuracy of the X\_tool in imaging the relative dip angle and thickness of the thin layer is verified. The conclusions are as follows:

(1) Employing a downhole LWD density tool, the gamma source is replaced with an X-ray source, and the source spacing of the X\_tool is optimized based on sensitivity to density measurement. The source spacing of the short- and long-spaced detectors is determined to be 138 mm and 260 mm, respectively. Compared to the G\_tool, the source spacings of the short- and long-spaced detectors are reduced by 24.5% and 31.5%, respectively, resulting in a

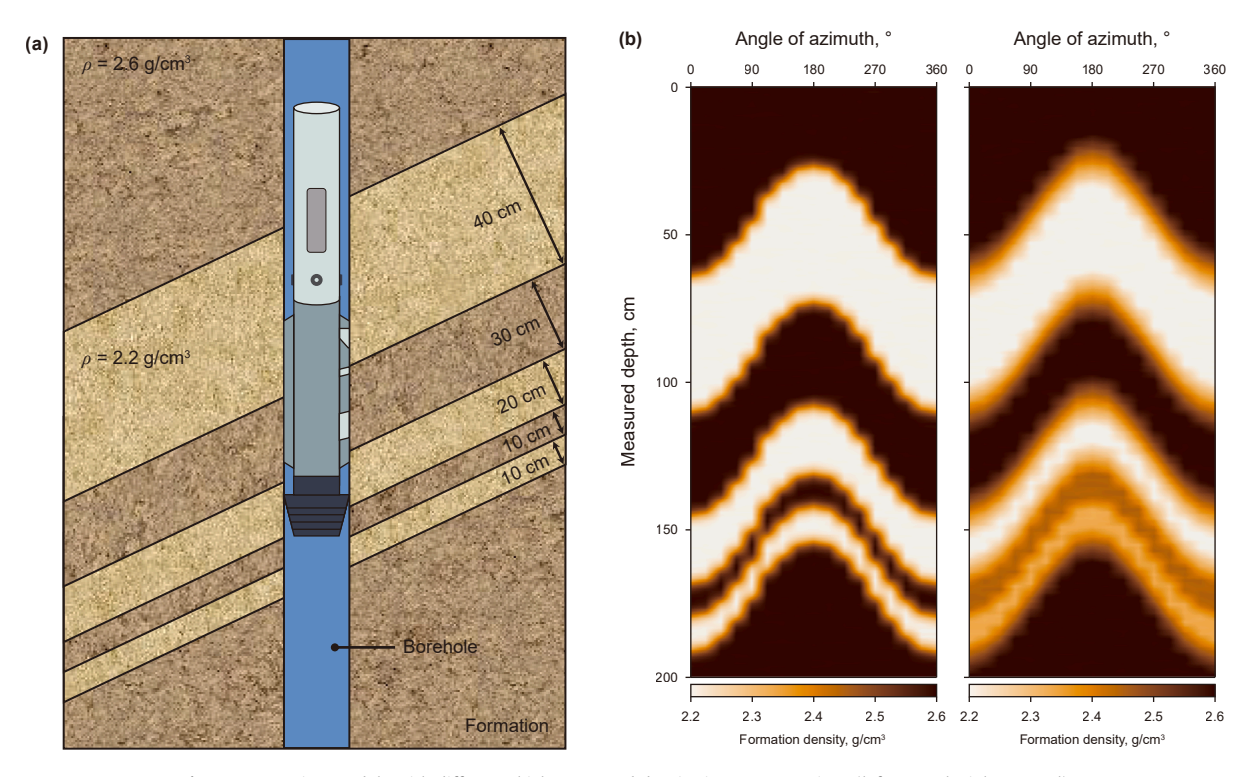


Fig. 10. Formation models with different thicknesses and density image comparison (left: X\_tool; right: G\_tool).

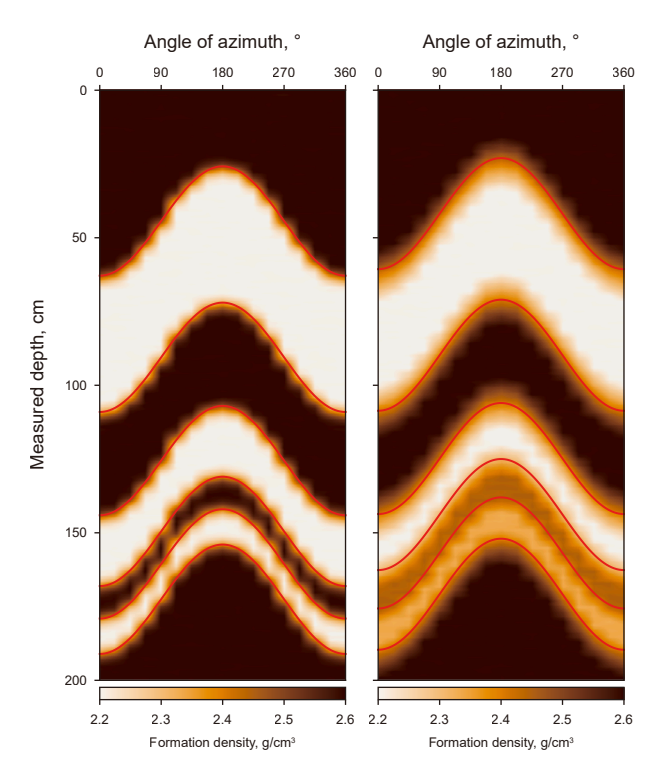


Fig. 11. Layer interface identification at different thickness (left: X\_tool; right: G\_tool).

significant improvement in vertical resolution—from 20 cm to 15 cm. In terms of formation densities, G\_tool results in an MAE of 0.0146 g/cm³ and an RMSE of 0.0148 g/cm³, in contrast to the results obtained by X\_tool, which show a higher accuracy with an MAE of 0.0140 g/cm³ and an RMSE of 0.0143 g/cm³.

 Table 4

 Comparison of thin layer thickness calculation results between the two tools.

Layer thickness, cm	X_tool	Relative error	G_tool	Relative error
40	40.15	0.375%	40.47	1.175%
30	30.48	1.600%	30.61	2.033%
20	20.53	2.650%	20.93	4.650%
10	10.72	7.200%	11.15	11.500%

**Table 5**MAE and RMSE between calculated and real thin layer thickness for two tools.

Error	X_tool	G_tool
MAE	0.470 cm	0.790 cm
RMSE	0.512 cm	0.834 cm

(2) The enhanced FOSM is employed to identify thin layer interfaces in density images. The X\_tool provides higher accuracy than the G\_tool in calculating thin layer thickness and relative dip angle. Specifically, as the layer thickness decreases, both X\_tool and G\_tool exhibit increasing errors in the estimation of thin layer thickness and relative dip angle. When the formation thickness is 10 cm, the relative errors of X\_tool and G\_tool are 7.20% and 11.50%, respectively. Overall, the RMSE of thin layer thickness estimation using X\_tool is reduced by 38.5% compared to G\_tool, and the RMSE of relative dip angle estimation is reduced by 33.7%, indicating that X\_tool offers higher accuracy in thin layer identification and further demonstrates the potential of the X-ray source for density measurement and thin layer identification.

Future work will focus on further optimizing the X-ray density imaging tool, particularly in terms of enhancing its vertical resolution and DOI. This involves refining the source spacing and

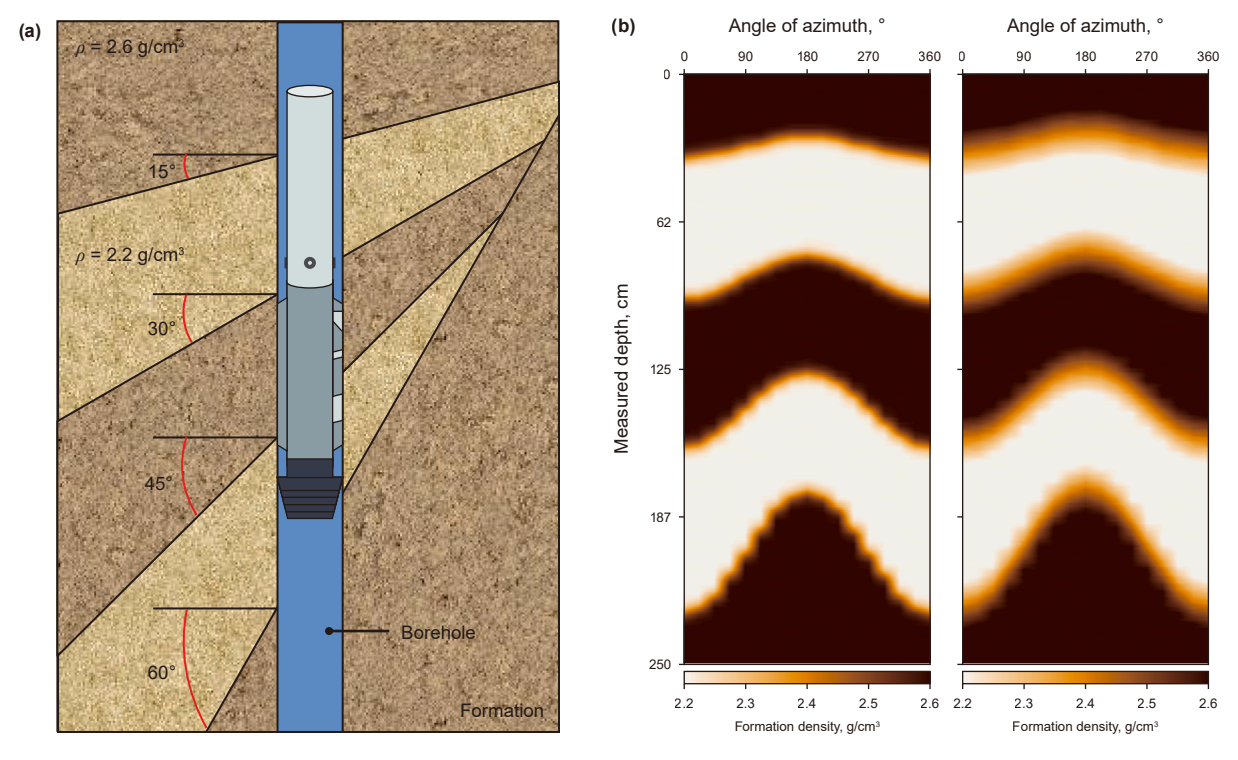
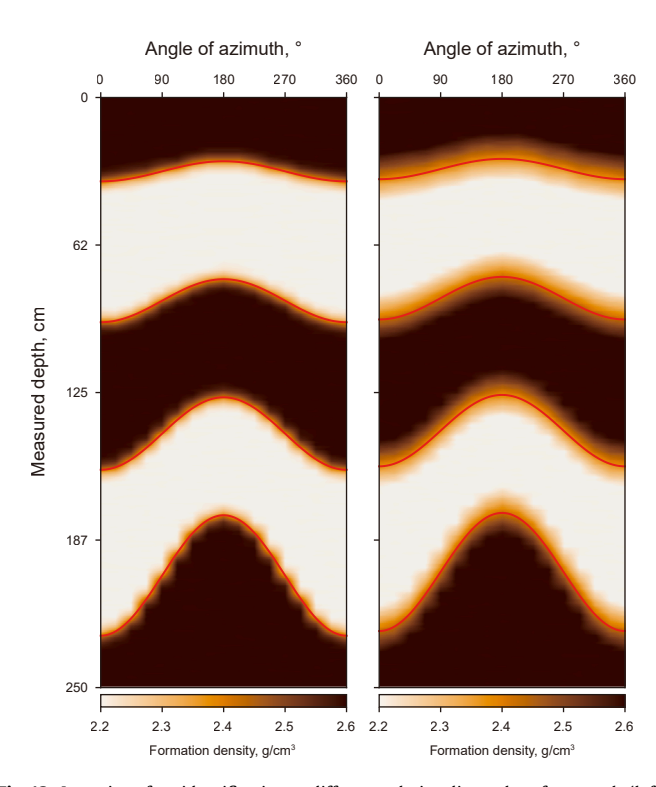


Fig. 12. Formation models with different relative dip angles and density image comparison (left: X\_tool; right: G\_tool).



 $\label{eq:Fig.13.} \textbf{Eayer interface identification at different relative dip angles of two tools (left: $X_{tool}$; right: $G_{tool}$).}$ 

detector layout to improve sensitivity in detecting thin layers. Additionally, further research will explore the integration of advanced signal processing algorithms and machine learning

**Table 6**Comparison between calculated and real relative dip angle for two tools.

Relative dip angle	X_tool	Relative error	G_tool	Relative error
15°	14.86°	0.933%	14.78°	1.467%
30°	29.57°	1.433%	28.96°	3.467%
45°	43.74°	2.800%	42.87°	4.733%
60°	57.83°	3.617%	56.92°	5.133%

**Table 7**MAE and RMSE between calculated and real relative dip angle for two tools.

Error	X_tool	G_tool
MAE	1.000°	1.618°
RMSE	1.275°	1.946°

techniques to enhance real-time formation evaluation. Experimental validation in field applications will also be conducted to assess the tool's performance under various borehole conditions and geological settings, ensuring its reliability and robustness for LWD density imaging.

# **CRediT authorship contribution statement**

**Wen-Bin He:** Writing – original draft, Methodology, Data curation, Conceptualization. **Ji-Lin Fan:** Investigation. **Qiong Zhang:** Writing – review & editing. **Ya Jin:** Data curation. **Wei Yuan:** Investigation. **Quan-Wen Zhang:** Conceptualization.

# **Conflict of interest**

The authors declared that they have no conflicts of interest to this work.

#### **Acknowledgements**

The authors would like to acknowledge the support of the National Natural Science Foundation of China (U23B20151 and 52171253).

#### References

- Agostinelli, S., Allison, J., Amako, K., et al., 2003. Geant4—a simulation toolkit. Nucl. Instrum. Methods Phys. Res. Sect. A Accel. Spectrom. Detect. Assoc. Equip. 506 (3), 250–303. https://doi.org/10.1016/S0168-9002(03)01368-8.
- Allison, J., Amako, K., Apostolakis, J., et al., 2006. Geant4 developments and applications. IEEE Trans. Nucl. Sci. 53 (1), 270–278. https://doi.org/10.1109/TNS.2006.869826.
- Allison, J., Amako, K., Apostolakis, J., et al., 2016. Recent developments in Geant4. Nucl. Instrum. Methods Phys. Res. Sect. A Accel. Spectrom. Detect. Assoc. Equip. 835, 186–225. https://doi.org/10.1016/j.nima.2016.06.125.
- Badruzzaman, A., 2014. An assessment of fundamentals of nuclear-based alternatives to conventional chemical source bulk density measurement. Petrophysics 55 (5), 415–434.
- Bai, G., Cao, B., 2014. Characteristics and distribution patterns of deep petroleum accumulations in the world. Oil Gas Geol. 35 (1), 19–25. https://doi.org/ 10.11743/ogg20140103.
- Best, D., Evans, M., Holenka, J., et al., 1995. Improved Formation evaluation using azimuthal porosity data while drilling. In: Proceedings of SPE Annual Technical Conference and Exhibition, SPE-30546-MS. https://doi.org/10.2118/30546-MS.
- Cheng, P., Zou, C.C., 2015. Improved Hough transform to detect planar geologic features in borehole images. J. Comput. Appl. 35 (6), 1726–1729. https://doi.org/10.11772/j.issn.1001-9081.2015.06.1726.
- Eldert, J.v., Schunnesson, H., Johansson, D., et al., 2020. Application of measurement while drilling technology to predict rock mass quality and rock support for tunnelling. Rock Mech. Rock Eng. 53 (3), 1349–1358. https://doi.org/10.1007/s00603-019-01979-2.
- Fan, J.L., Zhang, Q., Jin, Y., et al., 2024. Evaluation of cement density utilizing through-casing X-Ray logging method. Pet. Sci. 22 (3), 1041–1050. https://doi. org/10.1016/j.petsci.2024.11.004.
- Fisher, W.D., 1958. On grouping for maximum homogeneity. J. Am. Stat. Assoc. 53 (284), 789–798. https://doi.org/10.1080/01621459.1958.10501479.
- Geng, L., Zhaobiao, Y., Wei, G., et al., 2022. Characteristics of coal-measure gas reservoirs in thin interbedded marine-continental transitional facies and optimization of combined production: examples from the tucheng syncline in western guizhou. Nat. Resour. Res. 31 (3), 1503–1522. https://doi.org/10.1007/ s11053-022-10053-8.
- Gupta, K.D., Vallega, V., Maniar, H., et al., 2019. A deep learning approach for borehole image interpretation. In: Proceedings of SPWLA 60th Annual Logging Symposium, https://doi.org/10.30632/T60ALS-2019\_BB. SPWLA-2019-BB.
- Hu, W., Wei, Y., Bao, J., 2018. Development of the theory and technology for low permeability reservoirs in China. Petrol. Explor. Dev. 45 (4), 685–697. https:// doi.org/10.1016/S1876-3804(18)30072-7.
- John, A., Turvill, G.W.T., 1983. Formation evaluation: benefits of downhole logging while drilling: ABSTRACT. AAPG (Am. Assoc. Pet. Geol.) Bull. 67 (3), 560.
- Kang, W.L., Zhou, B.B., Issakhov, M., et al., 2022. Advances in enhanced oil recovery technologies for low permeability reservoirs. Pet. Sci. 19 (4), 1622–1640. https://doi.org/10.1016/j.petsci.2022.06.010.

- Lanning, E.N., Johnson, D.M., 1983. Automated identification of rock boundaries: an application of the Walsh transform to geophysical well-log analysis. Geophysics 48 (2), 197–205. https://doi.org/10.1190/1.1441458.
- Li, O.-Y., Wang, Y., Zhang, Q., et al., 2023. Parallel computing approach for efficient 3-D X-ray-simulated image reconstruction. Nucl. Sci. Tech. 34 (7), 101. https://doi.org/10.1007/s41365-023-01264-6.
- Mukherjee, B., Srivardhan, V., Roy, P.N.S., 2016. Identification of formation interfaces by using wavelet and Fourier transforms. J. Appl. Geophys. 128 (1), 140–149. https://doi.org/10.1016/j.jappgeo.2016.03.025.
- Pang, X.J., Wang, G.W., Kuang, L.C., et al., 2022. Prediction of multiscale laminae structure and reservoir quality in fine-grained sedimentary rocks: the Permian Lucaogou Formation in Jimusar Sag, Junggar Basin. Pet. Sci. 19 (6), 2549–2571. https://doi.org/10.1016/j.petsci.2022.08.001.
   Peng, X.L., Wang, M.W., Du, Z.M., et al., 2016. Upscaling and simulation of com-
- Peng, X.L., Wang, M.W., Du, Z.M., et al., 2016. Upscaling and simulation of composite gas reservoirs with thin-interbedded shale and tight sandstone. J. Nat. Gas Sci. Eng. 33, 854–866. https://doi.org/10.1016/j.jngse.2016.04.058.
- Shao, C.R., Cao, X.J., Chen, G.X., et al., 2013. A fast forward algorithm for LWD gamma-ray response and its geosteering application. Chin. J. Geophys. 56 (11), 3932–3942. https://doi.org/10.6038/cjg20131135.
- Simon, M., Tkabladze, A., Beekman, S., et al., 2018. A novel X-ray tool for true sourceless density logging. Petrophysics 59 (5), 565–587. https://doi.org/10.30632/PJV59N5-2018a1.
- Singhal, V., Ashok, P., Oort, E.v., et al., 2018. A novel X-ray based high pressure mass flow rate sensor for MPD operations. In: Proceedings of SPE Annual Technical Conference and Exhibition, SPE-191595-MS. https://doi.org/10.2118/191595-ms
- Sun, Q., Li, N., Duan, Y., et al., 2021. Logging-while-drilling formation dip interpretation based on long short-term memory. Petrol. Explor. Dev. 48 (4), 978–986. https://doi.org/10.1016/s1876-3804(21)60082-4.
- Wang, J., Huiszoon, C., Xu, L., et al., 2013. Quantitative study of natural gamma ray depth of image and dip angle calculations. In: Proceedings of SPWLA 54th Annual Logging Symposium, SPWLA-2013-BBB.
- Wang, Y., Zhang, Q., 2023. A characterization study on perovskite X-ray detector performance based on a digital radiography system. Nucl. Sci. Tech. 34 (5). https://doi.org/10.1007/s41365-023-01220-4.
- Wu, H., Li, Y., Jin, Y., et al., 2022. A design of source spacing of the X-ray density logging tool based on numerical simulation. Nucl. Tech. 45 (10), 43–50. https:// doi.org/10.11889/j.0253-3219.2022.hjs.45.100402.
- Xie, H., Omeragic, D., Shetty, S., et al., 2014. Improved consistency of inversion-based interpretation of LWD density images in complex horizontal well scenarios. In: Proceedings of SPWLA 55th Annual Logging Symposium, SPWLA-2014-BBBB.
- Yin, H., Guo, P., Mendoza, A., 2008. Comparison of processing methods to obtain accurate bulk density compensation and azimuthal density image from dual-detector gamma density measurements in high angle and horizontal wells. In: Proceedings of SPWLA 49th Annual Logging Symposium, SPWLA-2008-M.
- Yuan, X.Y., Deng, S.G., Li, Z.Q., et al., 2022. Deep-detection of formation boundary using transient multicomponent electromagnetic logging measurements. Pet. Sci. 19 (3), 1085–1098. https://doi.org/10.1016/j.petsci.2021.12.016.
- Zhang, Q., Ge, Y., Li, Y.-L., 2023. Source-less density measurement using an adaptive neutron-induced gamma correction method. Nucl. Sci. Tech. 34 (8), 125. https://doi.org/10.1007/s41365-023-01274-4.
- Zhu, G., Gao, M., Kong, F., et al., 2019. Application of logging while drilling tool in formation boundary detection and geo-steering. Sensors 19 (12). https://doi. org/10.3390/s19122754.